

Research Article

Enhanced Biocompatibility and Antibacterial Activity of Selective Laser Melting Titanium with Zinc-Doped Micro-Nano Topography

Fan Wu ^{1,2}, Ruogu Xu ^{1,2}, Xiaolin Yu ^{1,2}, Jiamin Yang ^{1,2}, Yun Liu ^{1,2},
Jianglin Ouyang ^{3,4}, Chunyu Zhang ^{3,4} and Feilong Deng ^{1,2}

¹Department of Oral Implantology, Guanghua School of Stomatology, Hospital of Stomatology, Sun Yat-Sen University, Guangzhou, China

²Guangdong Provincial Key Laboratory of Stomatology, Guangzhou, China

³Guangzhou Institute of Advanced Technology, Chinese Academy of Science, Guangzhou, China

⁴Guangzhou Janus Biotechnology Co., Ltd, Chinese Academy of Sciences, Guangzhou, China

Correspondence should be addressed to Feilong Deng; dengfl@mail.sysu.edu.cn

Received 28 January 2019; Accepted 2 April 2019; Published 21 May 2019

Academic Editor: Bo Tan

Copyright © 2019 Fan Wu et al. This is an open access article distributed under the Creative Commons Attribution License, which permits unrestricted use, distribution, and reproduction in any medium, provided the original work is properly cited.

Selective laser melting (SLM) titanium is a suitable material for use in customized implants. However, long-term implant survival requires both successful osseointegration and promising antibacterial characteristics. Native SLM titanium thus requires proper modifications to improve its bioactivity and antibacterial efficacy. Micro-arc oxidation (MAO) was conducted on sandblasted SLM substrate to form a microporous TiO₂ coating. Subsequently, hydrothermal treatment was applied to fabricate micro-nano zinc-incorporated coatings with different Zn content (1 mM-Zn and 100 μM-Zn). Surface characterization was performed using scanning electron microscopy, X-ray photoelectron spectroscopy, X-ray diffraction, a three-dimensional profilometer, and a contact angle measuring device. The osteoblast-like cell line MC3T3-E1, Subclone 14, was used in cell viability assays to evaluate adhesion, proliferation, and ALP activity. An antibacterial assay was conducted using *Streptococcus sanguinis* and *Fusobacterium nucleatum*. Zn-incorporated samples exhibited higher adhesion, proliferation, and differentiation than did SLM and MAO samples. 100 μM Zn samples exhibited the highest proliferation, and 1 mM-Zn samples manifested the highest ALP activity. In addition, Zn-incorporated samples exerted inhibitory effects on both *Streptococcus sanguinis* and *Fusobacterium nucleatum*. Combining micro-arc oxidation and hydrothermal treatment, we successfully fabricated a novel Zn-incorporated coating on a microporous SLM surface which possesses both outstanding bioactivity and antibacterial efficacy.

1. Introduction

Dental implants are the prior choice for patients suffering tooth loss due to predictable clinical outcomes [1]. However, patients whose conditions are complicated by irregular alveolar bone structure or extraction sockets are unsuitable to apply with such implants as their lengths, diameters, and tread parameters are predetermined and unmodifiable [2]. With the rapid development of computer-aided design (CAD) and additive manufacturing (AM), personalized implants can significantly simplify clinical procedure and shorten treatment times. Furthermore, customized implants

can minimize stress shielding and pressure-induced bone loss when compared to traditional implants [3, 4]. As manufacturing processes continue to advance, an increasing variety of customized implants are entering clinical use.

Selective laser melting (SLM), one of the most modern types of additive manufacturing (AM), is particularly well suited to fabricate customized implants or bone substitutes with free-form geometry [5–7]. Since the bone-implant interface is crucial to osseointegration, numerous studies have focused on evaluating the biocompatible properties of the SLM surface [8–11]. Compared to conventional machine-processed titanium, the biocompatibility of SLM substrate

remains controversial. Shaoki et al. reported that compared to the surface of machine-processed titanium, rates of osteoblast adhesion and differentiation were higher on an SLM surface but residual melted titanium particles decreased removal torque values [8]. Studies have also revealed that bacteria easily adhere to SLM substrate due to its rough and irregular surface [12, 13]. After SLM modifications both in vivo and in vitro (i.e., anodic oxidation, alkali-heat treatment, etc.), remarkable antibacterial properties, bone regeneration, and soft tissue adhesion were demonstrated with an SLM surface [12, 14, 15]. However, few of them possess both biocompatibility and antibacterial activity at the same time.

Micro-arc oxidation (MAO) has been widely used in the modification of biomaterial surfaces and confers a wide variety of biomechanical advantages [16, 17]. MAO-produced porous TiO₂ coating, incorporated with calcium and phosphorous, has been found to favorably influence osteoblast adhesion, proliferation, and differentiation [18]. In our previous study, we fabricated a rougher TiO₂ coating by combining sandblasting and acid etching technology with MAO, thus significantly enhancing biocompatibility [19]. Layer-by-layer manufacturing of native SLM specimens also resulted in a rough surface. Few studies, however, have focused on modifying the microscale surface of SLM specimens by MAO.

Peri-implantitis caused by bacteria is one severe complication that can eventually lead to implant failure [20]. Bacteria can not only aggregate on the implant surface, forming a biofilm and resisting antibacterial treatment, but also impede osseointegration and form alveolar absorption [21]. In order to enhance the antibacterial properties of biomaterials, various modification strategies have been applied, such as the loading of antibiotics, cross-linking of drugs, and construction of micro-nano topography [12, 22, 23]. Although antibacterial properties have improved, few methods with a focus on improving both osteogenesis and antibacterial properties have been reported.

Zinc, an essential trace element involved in multiple skeletal signaling pathways, reduces osteoclast resorption and improves osteoblast differentiation by regulating the expression of related genes [24, 25]. Biomaterials incorporating Zn have been found to exhibit remarkable osteogenic and antibacterial activity [26–30]. Among the different Zn compounds, ZnO exhibits powerful antibacterial properties due to its membrane-damaging effects, generation of reactive oxygen species (ROS), and release of Zn ions [31]. However, a high concentration of Zn not only is toxic to bacteria but also causes damage to human cells [32]. It is thus vital to appropriately adjust the concentration of Zn in any biomaterial, enough to inhibit bacterial adhesion and reproduction while conferring no cytotoxicity.

In this study, we modified the surface of an SLM substrate using MAO thus forming a microporous morphology. We further doped Zn ions onto the MAO surface by hydrothermal treatment, constructing a micro-nano topography on the SLM specimen. Surface characterization was performed by scanning electron microscopy (SEM), energy-dispersive spectroscopy (EDS), X-ray photoelectron spectroscopy (XPS), X-ray diffraction (XRD), a 3D profilometer, and a

contact angle measuring device. Antibacterial activity was assessed by oral pathogenic bacterial species, including *S. sanguinis* and *F. nucleatum*. Cytocompatibility of the modified SLM surface was evaluated by characterizing the morphology, attachment, proliferation, and differentiation of osteoblast-like cells (MC3T3-E1). Despite that MAO has been widely used in implant surface modification, here we present a novel method to combine MAO and zinc element of the SLM substrate, which both improves biological performance and enhances antibacterial efficacy with the ultimate aim of improving customized dental implant success rates and reducing the risk of peri-implant inflammation.

2. Materials and Methods

2.1. Specimen Preparation and Treatment. The SLM specimens were manufactured as described previously [12, 15]. Briefly, round-disk samples (diameter, 10 mm; thickness, 1 mm) were designed by SolidWorks® 12.0 (SolidWorks Corp, USA). According to the data, specimens were fabricated by an SLM machine (SLM125HL, SLM Solutions GmbH, Germany) using commercial grade II titanium powders (Western BaoDe, China) as raw materials. The main characteristics of SLM machine were as follows: the maximum laser power is 145 W, the layer thickness is 30 μm, the laser scanning speed is 355 mm/s, the laser spot size is 50 μm, and the hatch space is 45 μm. All SLM titanium specimens were ultrasonically cleaned with acetone, ethanol, and deionized water for 15 min each time considered as SLM samples. To eliminate the residual titanium spheres and the native oxide layer of surface, some of the SLM samples were sandblasted by ZrO₂ particles (diameter, 250 μm) and then chemically polished in 5% hydrofluoric acid solution for 30 sec. Subsequently, they were ultrasonically cleaned and dried. MAO was conducted in an electrolyte solution with 0.02 M glycerophosphate disodium salt pentahydrate (C₃H₇Na₂O₆P·5(H₂O)) and 0.05 M calcium acetate monohydrate (Ca(CH₃COO)₂·H₂O) using a pulsed DC power supply (MHWYDM750-20, Nenghua Electrical Co., China). Frequency, duty, voltage, and time were 100 Hz, 26%, 410 V, and 6 min, respectively. These specimens were considered as MAO samples. After MAO, parts of the MAO samples were hydrothermally treated in a Teflon-lined autoclave containing 1 mM and 100 μM of zinc acetate (Zn(CH₃COO)₂) at 200°C for 3 h. These further treated specimens we termed as 1 mM-Zn and 100 μM-Zn samples. Each sample was ultrasonicated in deionized water after every single treatment step. Samples were divided into four groups, namely SLM, MAO, 1 mM-Zn, and 100 μM-Zn.

2.2. Specimen Characterization. Surface topographies were observed using field-emission scanning electron microscopy (FE-SEM, SU70, Hitachi, Japan). Chemistry compositions of surface were analyzed using an electronic differential system (EDS) equipped with FE-SEM and X-ray photoelectron spectroscopy (XPS, ESCALAB 250Xi, Thermo Scientific, USA). Crystallinity of the coatings was evaluated using an X-ray diffractometer (XRD, PANalytical B.V., X'Pert-PRO, Holland) fitted with a Cu Kα (λ = 0.154056 nm) at 40 kV

and 40 mA in the range from 20° to 80° (2θ) with a step size of 0.02. Surface profiles and roughness were scanned with a 3D profilometer (BMT EXPERT, Germany). The static contact angles were determined by an optical contact angle measuring device (OCA40 Micro, Data Physics, Germany). To determine Zn-related characteristics of each sample, 1 mM-Zn and 100 μ M-Zn specimens were immersed in 3 ml phosphate-buffered saline (PBS, Gibco, USA) at 37°C for 1, 4, 7, and 14 days successively. At predetermined time points, the collected PBS that contained Zn was analyzed by inductively coupled plasma mass spectrometry (ICP-MS, Agilent 7900, Agilent Technologies Inc., USA).

2.3. Cell Culture. The preosteoblastic cell line MC3T3-E1 subclone 14 (Shanghai Cellular Institute of the Chinese Academy of Sciences, China) was cultured in α -MEM medium (Gibco, USA) containing 10% fetal bovine serum (FBS, Gibco, USA) and 1% antibiotic/antimycotic solution (Gibco, USA) at 37°C under a humidified atmosphere of 5% CO₂. The culture medium was changed every 2 days to remove suspended cells.

2.4. Cell Proliferation Activity Assay. Cell counting kit-8 assay (CCK-8, Dojindo, Japan) was used to evaluate the cell proliferation of MC3T3-E1 quantitatively [33]. MC3T3-E1 cells were seeded on sample surfaces at a density of 1×10^4 cells ml⁻¹ in 48-well plates and cultured for 1, 4, and 7 days. At these predetermined time points, each sample was rinsed three times with PBS. Adherent cells were incubated with 500 μ l 10% CCK-8 mixed with culture medium for 2 h at 37°C. The optical density (OD) was measured at 450 nm on an ELISA reader (Tecan, SUNRISE, Switzerland).

2.5. Alkaline Phosphatase (ALP) Activity Assay. MC3T3-E1 cells were seeded on sample surfaces at a density of 2×10^4 cells ml⁻¹ in 48-well plates. After culturing with osteogenic medium (α -MEM medium supplemented with 10 mM β -glycerophosphate, 0.05 mM l-ascorbic acid, and 100 mM dexamethasone) for 14 days, cells were lysed by 0.1% Triton X-100 at 4°C overnight and an ALP assay kit (Jiancheng, China) was subsequently used to evaluate the ALP activity measured at an OD value of 520 nm. A protein assay kit (BCA, Beyotime, China) was used to normalize readings to total protein content measured at a wavelength of 562 nm [33].

2.6. Cell Morphology. MC3T3-E1 cells were seeded on sample surfaces at a density of 1×10^4 cells ml⁻¹ in 48-well plates for 2 h and fixed in 3% glutaraldehyde solution at 4°C for 10 h. After dehydration in increasing grades of ethanol (50%, 75%, 90%, 95%, and 100%), drying, and sputter-coating with platinum, samples were observed under FE-SEM.

2.7. Bacterial Culture. *Streptococcus sanguinis* (ATCC 10556) and *Fusobacterium nucleatum* (ATCC 10953) were used to evaluate the antibacterial activity. *S. sanguinis* and *F. nucleatum* were seeded onto brain heart infusion (BHI) agar and blood agar plates (Huankai Microbial, China), respectively. After incubation under anaerobic conditions at 37°C for 24 and 48 h, a single colony of *S. sanguinis* was placed into the

BHI medium and *F. nucleatum* was placed into the BHI medium supplemented with hemin (0.5 mg/ml) and menadi-one (0.1 mg/ml). After incubating under anaerobic conditions for 24 h, bacterial suspensions were diluted to 1×10^7 CFU ml⁻¹ using the McFarland scale for bacterial adhesion and antibacterial testing. Each sample was placed in a 24-well plate and immersed in 1 ml diluted bacterial suspension for 24 h under anaerobic conditions.

2.8. Bacterial Morphology. Bacterial morphology on all specimens was evaluated using FE-SEM after incubation for 24 h. Samples were rinsed three times with PBS to remove any suspended bacteria. Each sample was immersed in 3% glutaraldehyde at 4°C for 10 h and then dehydrated in a graded series of ethanol solutions (50%, 75%, 90%, 95%, and 100%) for 10 min. All samples were sputter-coated with platinum.

2.9. Antibacterial Test. To determine the antibacterial characteristics of tested materials, samples were rinsed with PBS after 24 h of incubation and transferred into 3 ml PBS. The density of surviving microorganisms was quantified using an ELISA reader at a wavelength of 600 nm in the collected culture medium. The *S. sanguinis* and *F. nucleatum* that adhered to each sample were detached by ultrasonic vibration for 15 min (20 W, 80 kHz) and a subsequent 15 s vortex. After a 3000-fold dilution with PBS, 100 μ l of diluted suspension was spread onto BHI agar and blood agar plates, respectively. After incubation in an anaerobic environment at 37°C for 48 h, bacterial colony counts of *S. sanguinis* and *F. nucleatum* were obtained. Antibacterial effectiveness of adhered *S. sanguinis* and *F. nucleatum* were calculated using the antibacterial ratio % (equation (1)), where *A* represents the bacterial count in contact with SLM samples and *B* represents experiment samples (MAO, 1 mM-Zn, and 100 μ M-Zn samples).

$$\text{Antibacterial ratio\%} = \frac{A - B}{A} \times 100\%. \quad (1)$$

2.10. Statistical Analysis. SPSS 24.0 software (SPSS Inc., USA) was used to perform statistical analysis. A four-group comparison was measured via one-way ANOVA followed by a Bonferroni post hoc test for multiple comparison (significance, $P < 0.05$). All the experiments were performed in triplicate, and all the data were expressed as means \pm standard deviation (SD).

3. Results

3.1. Surface Characterization. Surface sample topographies are shown in Figure 1. Some residual unmelted titanium spheres were found on the rough SLM surface while porous structures 2–5 μ m in size were found formed on MAO samples. The incorporation of Zn and subsequent hydrothermal treatment did not alter porous surface morphology. On high-power magnification, SLM samples revealed irregular grooves and dots. MAO samples revealed a rather smooth surface while nanoparticles appeared distributed throughout the hydrothermally treated samples. The 1 mM-Zn samples revealed a relatively smaller nanoparticle size (20–30 nm),

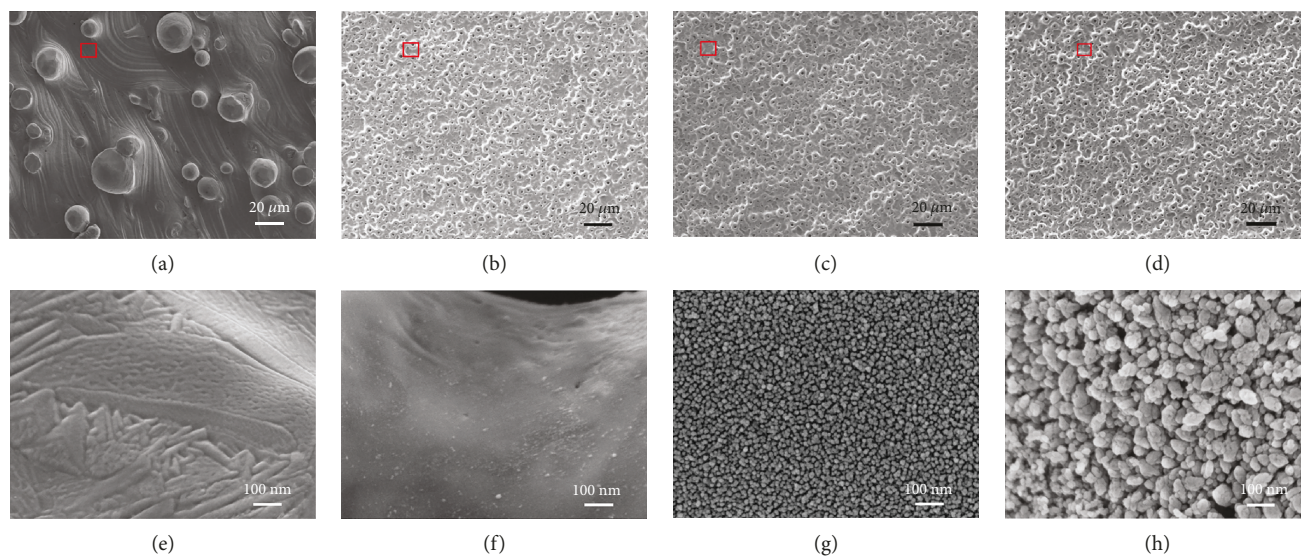


FIGURE 1: SEM images showing surface topographies of each group (scale bar of (a-d) = 20 μm , scale bar of (e-h) = 100 nm). Low magnifications of SLM, MAO, 1 mM-Zn, and 100 μM -Zn samples (a-d); high magnification of SLM, MAO, 1 mM-Zn, and 100 μM -Zn samples in the red boxes location (e-h).

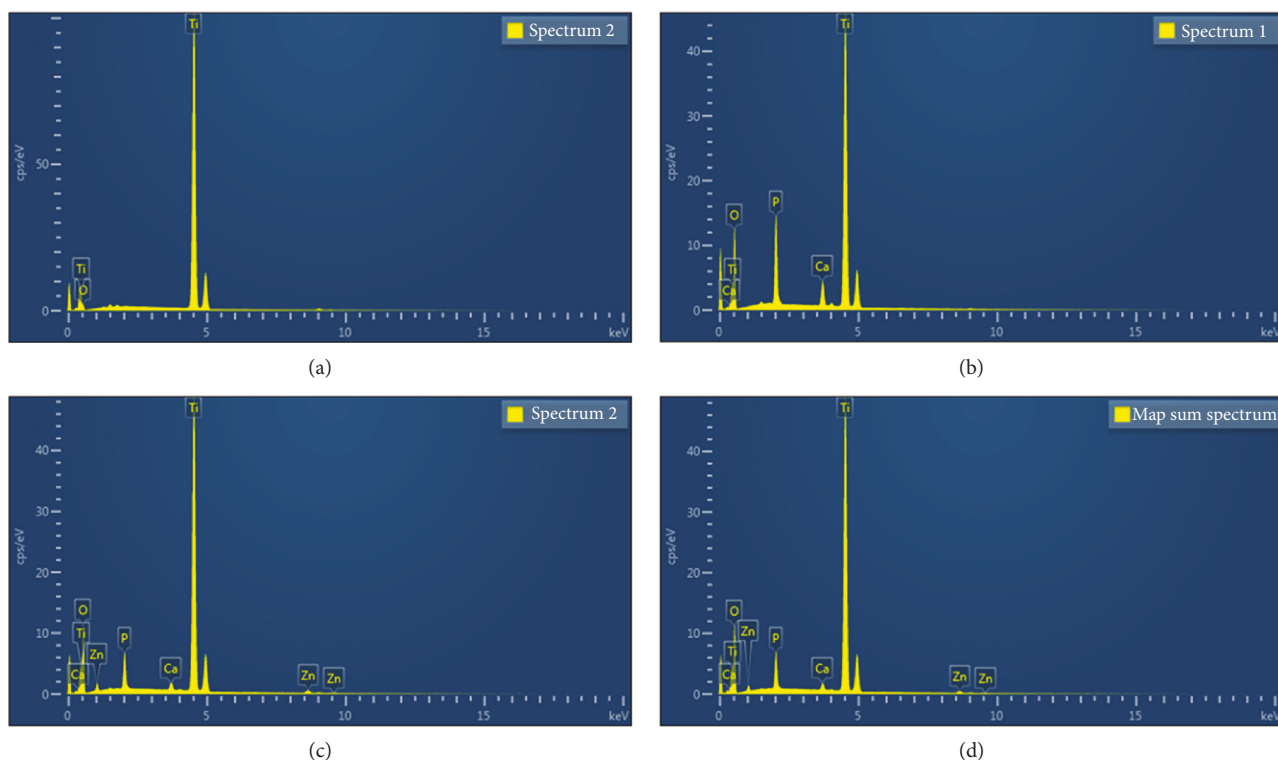


FIGURE 2: EDS spectra of the samples. SLM samples only consisted of titanium and oxygen elements (a); MAO samples were composited with titanium, oxygen, calcium, and phosphorus elements (b); titanium, oxygen, different contents of zinc, less calcium, and phosphorus elements existed on the surface of 1 mM-Zn and 100 μM -Zn samples (c, d).

but their shapes were more uniform than on the surfaces of 100 μM -Zn samples (30–60 nm).

Sample EDS spectra are shown in Figure 2, and surface elemental compositions are shown in Table 1. Ti and O were observed on all samples. The elements Ca and P were noted on all MAO samples. Compared to MAO samples,

Ca and P content was decreased in both 1 mM-Zn and 100 μM -Zn samples.

XRD patterns (Figure 3) confirmed that single-phase anatase TiO_2 formed during MAO and MAO with hydrothermal treatment in $\text{Zn}(\text{CH}_3\text{COO})_2$ solution. No Zn- or CaP-containing species were detected by XRD analysis, likely

TABLE 1: EDS analysis of the elemental composition of each sample (wt. %).

Samples	Ti	O	Ca	P	Zn
SLM	89.91	10.09	—	—	—
MAO	46.88	44.27	2.44	6.41	—
1 mM-Zn	51.53	42.49	0.79	2.96	2.23
100 μ M-Zn	51.95	42.71	0.74	3.02	1.58

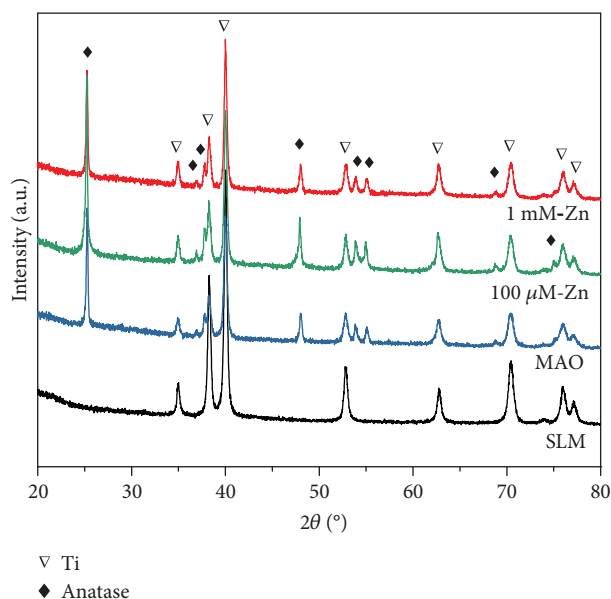


FIGURE 3: XRD spectra of each sample. Titanium and anatase were detected on SLM, MAO, 1 mM-Zn, and 100 μ M-Zn samples.

due to their low content or amorphous form in these as-prepared samples.

XPS analysis (Figure 4) was performed to evaluate the surface chemical states of as-prepared samples. In MAO samples, two peaks (at 532.5 and 530.9 eV) were observed in O 1s XPS spectrum, assigned to the binding energy of O in hydroxyl and lattice oxygen. Peaks at 458.6 eV and 464.3 eV in the Ti 2p XPS spectrum were, respectively, assigned to $Ti^{4+} 2p_{3/2}$ and $Ti^{4+} 2p_{1/2}$. These XPS findings were in agreement with XRD analysis, confirming that the TiO_2 formed during the synthetic procedure. Peaks at 347.6 and 351.2 eV in Ca 2p XPS spectrum, respectively, corresponded to $Ca^{2+} 2p_{3/2}$ and $Ca^{2+} 2p_{1/2}$. The binding energy at 133.8 eV for P 2p was assigned to the p^{5+} in $Ca_{10}(PO_4)_6(OH)_2$ [34]. Compared to MAO samples, no obvious changes in the binding energy of P 2p and Ca 2p were observed in the 100 μ M sample. The Zn 2p_{3/2} at 1021.5 eV and 2p_{1/2} at 1044.5 eV suggested that Zn^{2+} content was successfully coated on the surface of TiO_2 . The O 1s could additionally be split into three peaks: 532.5 eV for hydroxyl in $Ca_{10}(PO_4)_6(OH)_2$, 529.9 eV for lattice oxygen in TiO_2 , and 530.9 eV for lattice oxygen in ZnO. The greater binding energy of Zn-O than that of Ti-O is attributed to the greater electronegativity of Zn (1.65) than Ti (1.54). Our findings imply that the layer coating TiO_2 was composed of ZnO and $Ca_{10}(PO_4)_6(OH)_2$.

Surface profile images and sample hydrophilicity as determined by water contact angle analysis are shown in Figure 5; findings are shown in Table 2. SLM samples exhibited the highest Ra value of 6.96 μ m. The Ra value of MAO, 1 mM-Zn, and 100 μ M-Zn samples were 1.85, 1.74, and 1.85 μ m, respectively, and were smoother than SLM samples. The water contact angles of SLM and MAO samples were 59.07° and 15.7°, respectively, while 1 mM-Zn and 100 μ M-Zn samples exhibited total hydrophilicity and their water contact angles could not be measured.

The Zn ion concentration released in PBS was measured by ICP-MS (Figure 6). During immersion in PBS for 14 days, both Zn-incorporated samples released Zn ions continuously at a low level. The total amount of Zn ions in 1 mM-Zn samples was higher than in 100 μ M-Zn samples which were in accordance with the surface EDS analysis above.

3.2. Cell Proliferation and Morphology. Figure 7 shows results of MC3T3-E1 proliferation on each sample. At days 1, 4, and 7, MAO, 1 mM-Zn, and 100 μ M-Zn samples were found to have greater proliferation than were SLM samples. The 100 μ M-Zn group showed higher proliferation than did other groups on the 1st and 7th days. MC3T3-E1 cells exhibited a spindle and elongated shape on SLM surfaces but cellular morphology on MAO, 1 mM-Zn, and 100 μ M-Zn samples extensively varied (Figure 8).

3.3. Alkaline Phosphatase (ALP) Activity. The osteogenic function of MC3T3-E1 cells was evaluated by analyzing ALP activity after 14 days of culture (Figure 9). SLM samples performed poorly compared to the other three groups in the ALP activity test. ALP activities in 1 mM-Zn and 100 μ M-Zn groups were statistically significantly higher than in the MAO group, and the 1 mM-Zn group was found to have the highest statistically significant level (1 mM-Zn > 100 μ M-Zn > MAO > SLM).

3.4. Antibacterial Activity. Antibacterial findings are detailed in Figure 10. Both *S. sanguinis* and *F. nucleatum* adhered to SLM samples at rates significantly higher than in other groups. The antibacterial efficacy of MAO samples against adhered *F. nucleatum* was $18.32 \pm 4.88\%$; however, no antibacterial effects of MAO samples against *S. sanguinis* were found despite SLM samples possessing the roughest surface. Samples incorporated with Zn significantly enhanced antibacterial activity with 1 mM-Zn group samples exhibiting the most effective inhibition of both bacterial species. Morphologies of *S. sanguinis* and *F. nucleatum* captured by SEM (Figure 11) revealed how samples incorporated with Zn also reduced bacterial adhesion. Lower quantities of *S. sanguinis* and *F. nucleatum* were found on 1 mM-Zn and 100 μ M-Zn sample surfaces, while organisms found adhered to SLM and MAO samples were densely aggregated.

Bacterial density in Zn-incorporated sample culture media was statistically significantly lower than in SLM and MAO groups (Figure 12). Compared with 100 μ M-Zn samples, bacterial density in 1 mM-Zn samples was markedly lower, implying that bacterial density gradually decreased as the concentration of Zn ions in supernatant increased.

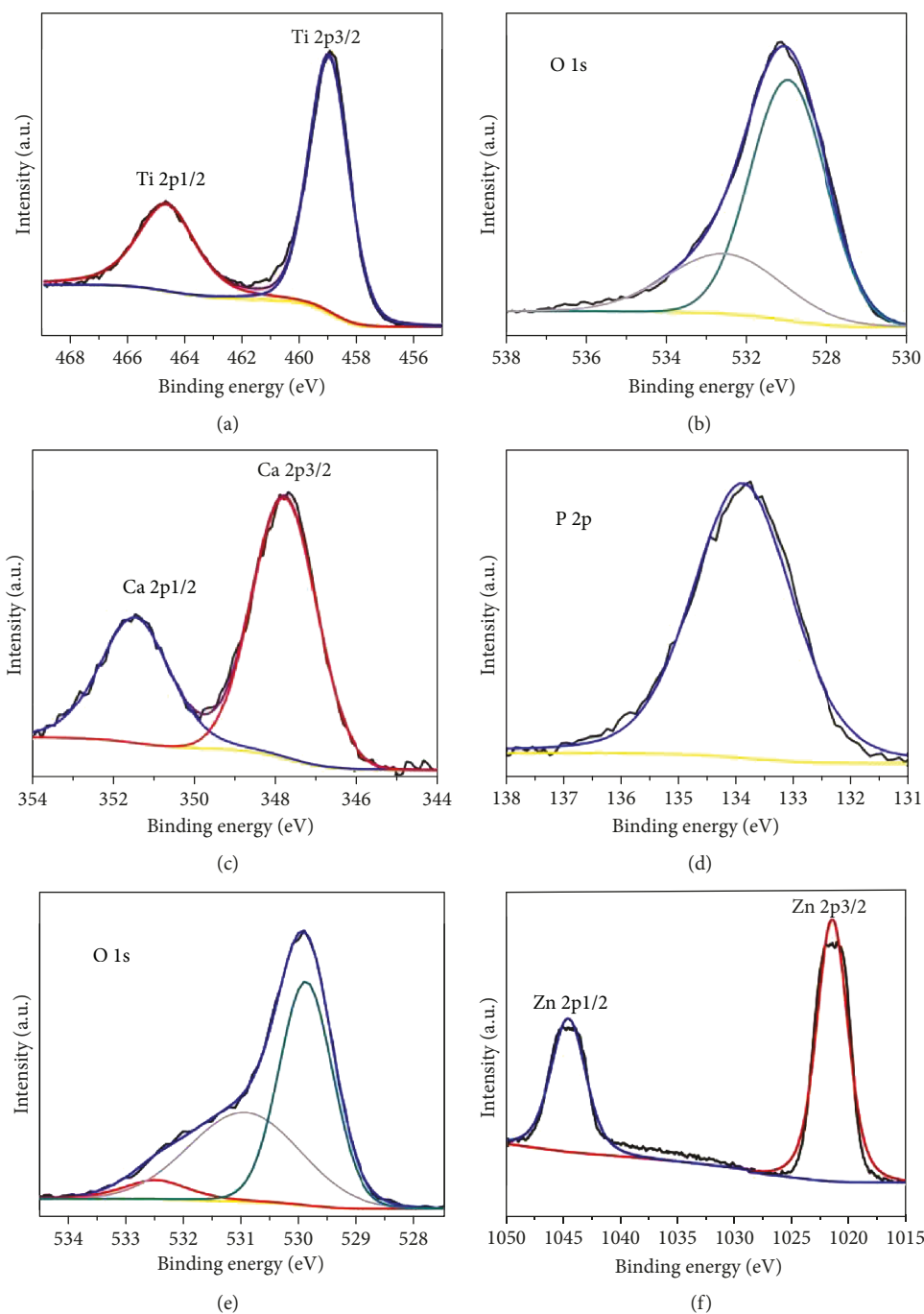


FIGURE 4: XPS spectra of MAO and 100 μM -Zn samples. Ti 2p (a), O 1s (b), Ca 2p (c), and P 2p (d) of MAO sample; O 1s (e) and Zn 2p (f) of the 100 μM -Zn sample.

4. Discussion

Surface modification of titanium can significantly enhance the osteogenesis and antibacterial efficacy [35–38]. In this study, we fabricated a novel Zn-incorporated TiO_2 coating by MAO and subsequent hydrothermal treatment producing micro-nano topography on an SLM surface.

Surface roughness plays an important role in the adherence and proliferation of cells and bacteria. Albrektsson and Wennerberg demonstrated that dental implants with moderately rough surfaces ($1.0 \mu\text{m} < \text{Ra} < 2.0 \mu\text{m}$) evoke

stronger bone responses than do smoother or rougher surfaces [39]. Rønold and Ellingsen [40] and Rønold et al. [41] proved that bone bonding forces increase with rougher surfaces to a threshold of $3.62\text{--}3.90 \mu\text{m}$ (range: $0.63 \mu\text{m}\text{--}11.03 \mu\text{m}$). Increased roughness also promotes the formation and maturation of biofilms, especially when the Ra value exceeds $0.2 \mu\text{m}$ [42, 43]. Due to the layer-by-layer manufacturing process and unmelted spheres, the original SLM specimens we fabricated had an Ra value of $6.96 \mu\text{m}$. In order to decrease substrate roughness, we applied sand-blasting and acid polishing to eliminate residual particles

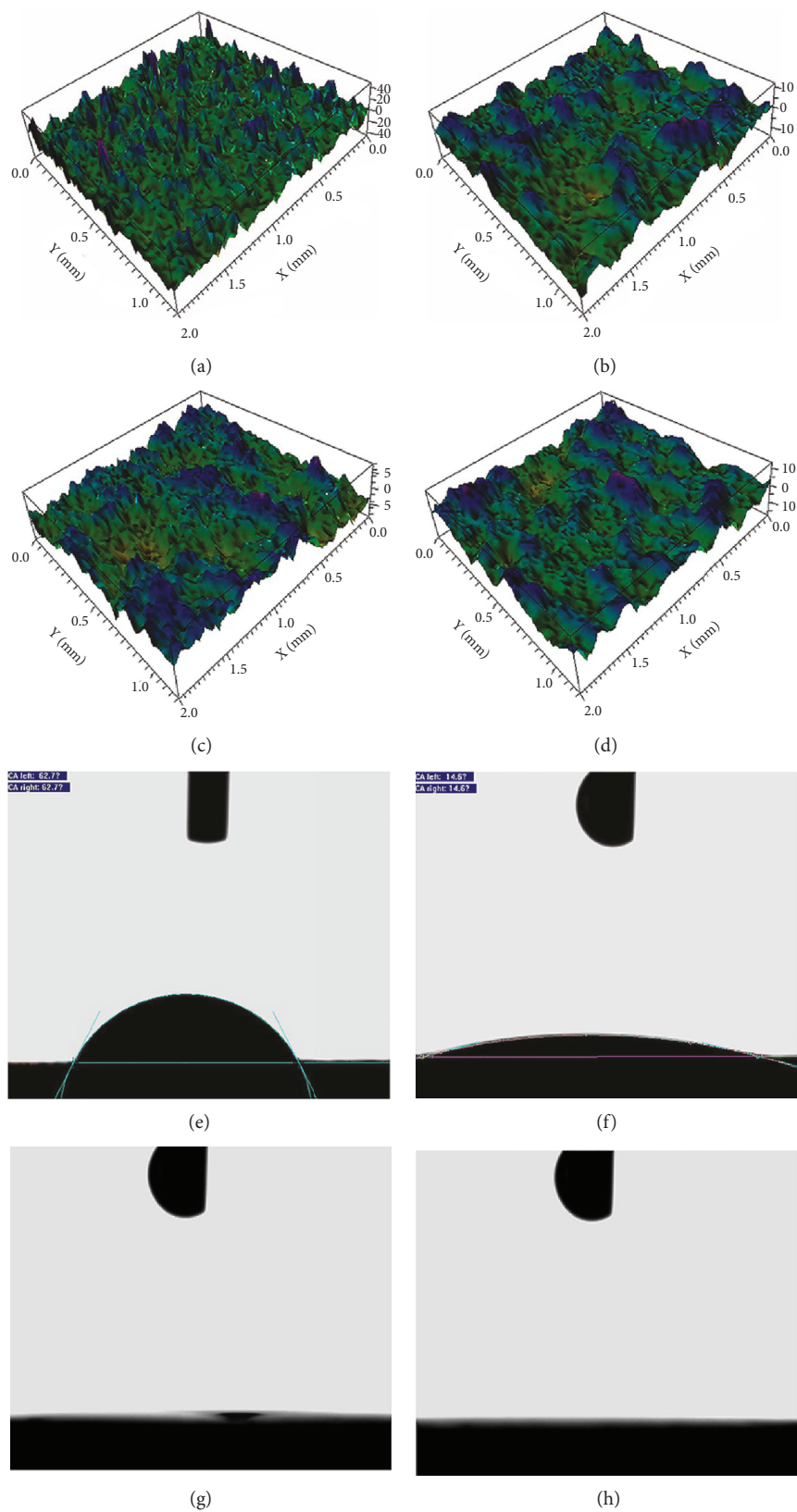


FIGURE 5: Surface profiles and contact angles of each sample. Surface roughness profiles of SLM, MAO, 1 mM-Zn, and 100 μ M-Zn samples (a–d); MAO samples (f) showed better hydrophilia than did SLM samples (e); 1 mM-Zn and 100 μ M-Zn samples (g and h) showed total hydrophilicity.

TABLE 2: Surface roughness and water contact angles of each sample.

Samples	Ra (μm)	Rq (μm)	Contact angle ($^\circ$)
SLM	6.96 ± 0.71	9.56 ± 0.85	59.07 ± 3.18
MAO	1.85 ± 0.17	2.36 ± 0.25	11.03 ± 6.44
1 mM-Zn	1.74 ± 0.22	2.14 ± 0.3	0.00 ± 0.00
100 μM -Zn	1.85 ± 0.12	2.33 ± 0.11	0.00 ± 0.00

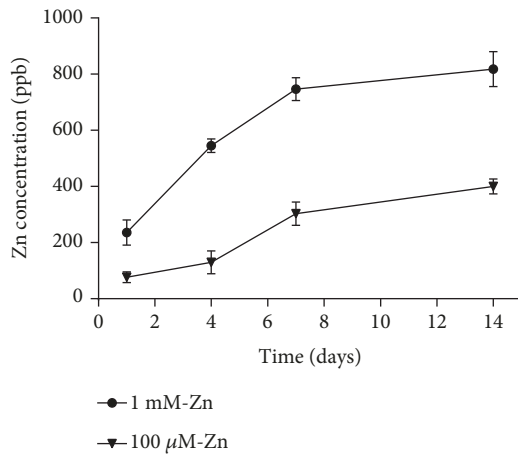


FIGURE 6: Zn ion concentration released from each sample of different immersion time.

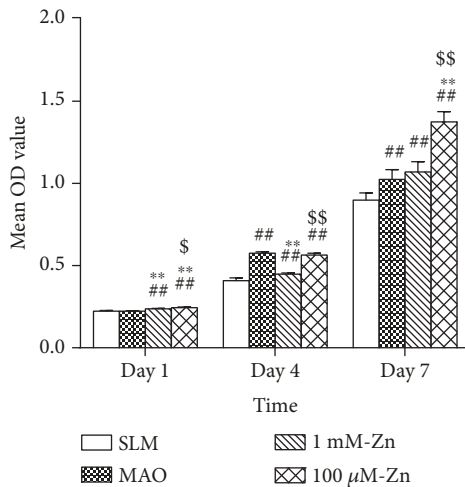


FIGURE 7: Cell proliferation of MC3T3-E1 cells on the surface of each sample after 1, 4, 7 days. # $P < 0.05$ and ## $P < 0.01$ compared with SLM; * $P < 0.05$ and ** $P < 0.01$ compared with MAO; \$ $P < 0.05$ and \$\$ $P < 0.01$ compared with 1 mM-Zn.

prior to the MAO procedure and subsequent hydrothermal treatment. The Ra values of MAO, 1 mM-Zn, and 100 μM -Zn samples were 1.85 μm , 1.74 μm , and 1.85 μm , respectively, all within the range of optimal implant surface roughness.

Surface wettability is another important physicochemical property of biomaterials. Previous studies have shown that the hydrophilicity of surfaces influences both cellular and

bacterial morphology, adherence, and proliferation. Compared to hydrophobic surfaces, hydrophilic surfaces significantly promote cellular attachment and proliferation [44]. In addition, implants with significant wettability decrease the postimplant healing period and accelerate early osseointegration [45–47]. MAO, 1 mM-Zn, and 100 μM -Zn samples were all evaluated with high surface hydrophilicity by water contact angle analysis. Most oral bacteria, including *S. sanguinis* and *F. nucleatum*, thrive better on surfaces with high wettability [48, 49]. Further modifications should be applied to improve antibacterial effects.

Zn-incorporated coatings are well known to possess strong bacteriostatic properties, effectively inhibiting adhesion and proliferation of a wide variety of bacteria [26–28]. The ZnO in coatings also exerts antibacterial effects by ROS generation (i.e., H_2O_2 , OH^- , and O_2^{2-}) [50]. In addition, free Zn ions also penetrate bacterial membranes and cause DNA damage [51]. Research has proven that dental implant failure was commonly associated to dental plaque formation. As an early colonizer of dental plaques, *S. sanguinis* can attach directly to the surface of implants and facilitate the adhesion of later colonized bacteria, which eventually transfer the plaque to a “mature” community with high levels of Gram-negative anaerobic filamentous organisms [52, 53]. *F. nucleatum*, one of the most common pathogens associated with peri-implantitis, is a later colonizer during biofilm formation [54]. We also noted that the antibacterial efficacy towards both *S. sanguinis* and *F. nucleatum* depended on the content of Zn within coatings. This is likely due to coatings with a higher Zn content releasing a greater quantity of Zn ions and more strongly inhibiting bacterial adhesion and proliferation by mechanisms such as ROS formation. In contrast to *S. sanguinis*, colony counts of *F. nucleatum* adhered to MAO samples were significantly lower than those of SLM samples. This difference is likely due to the catalytic effect of anatase in MAO coatings [55].

As a trace element, Zn plays a crucial role in the process of bone regeneration. Various studies have reported that biomaterials incorporating Zn exhibited promising biological characteristics both in vivo and in vitro [29, 30]. Zn enhances osteoblastic adhesion and proliferation by upregulating the expression of FAK and integrin [56]. Zn exerts positive effects on bone formation by promoting the expression of genes involved in osteogenesis such as Runx2, ALP, OCN, and Col-I [30]. Moreover, Zn also decreases bone loss by suppressing osteoclast differentiation via inhibition of RANK expression [57]. Importantly, Zn can only confer favorable cytocompatibility properties and minimal cytotoxicity at an extremely low concentration. Yamamoto et al. demonstrated that the half maximal inhibitory concentration (IC_{50}) of ZnCl_2 is 9.28×10^{-5} mol/l (equals to 12.65 ppm of Zn ions) [58]. Ito et al. additionally reported that no cytotoxicity was observed at a Zn ion concentration of 3 ppm [59]. As shown in Figure 6, Zn ions released from 1 mM-Zn and 100 μM -Zn samples accumulated to levels lower than 3 ppm and thus remained in a relatively safe range.

In our present experiment, MC3T3-E1 cells were used to test Zn-incorporated coating viability. SEM images revealed that both 1 mM-Zn and 100 μM -Zn samples were favorable

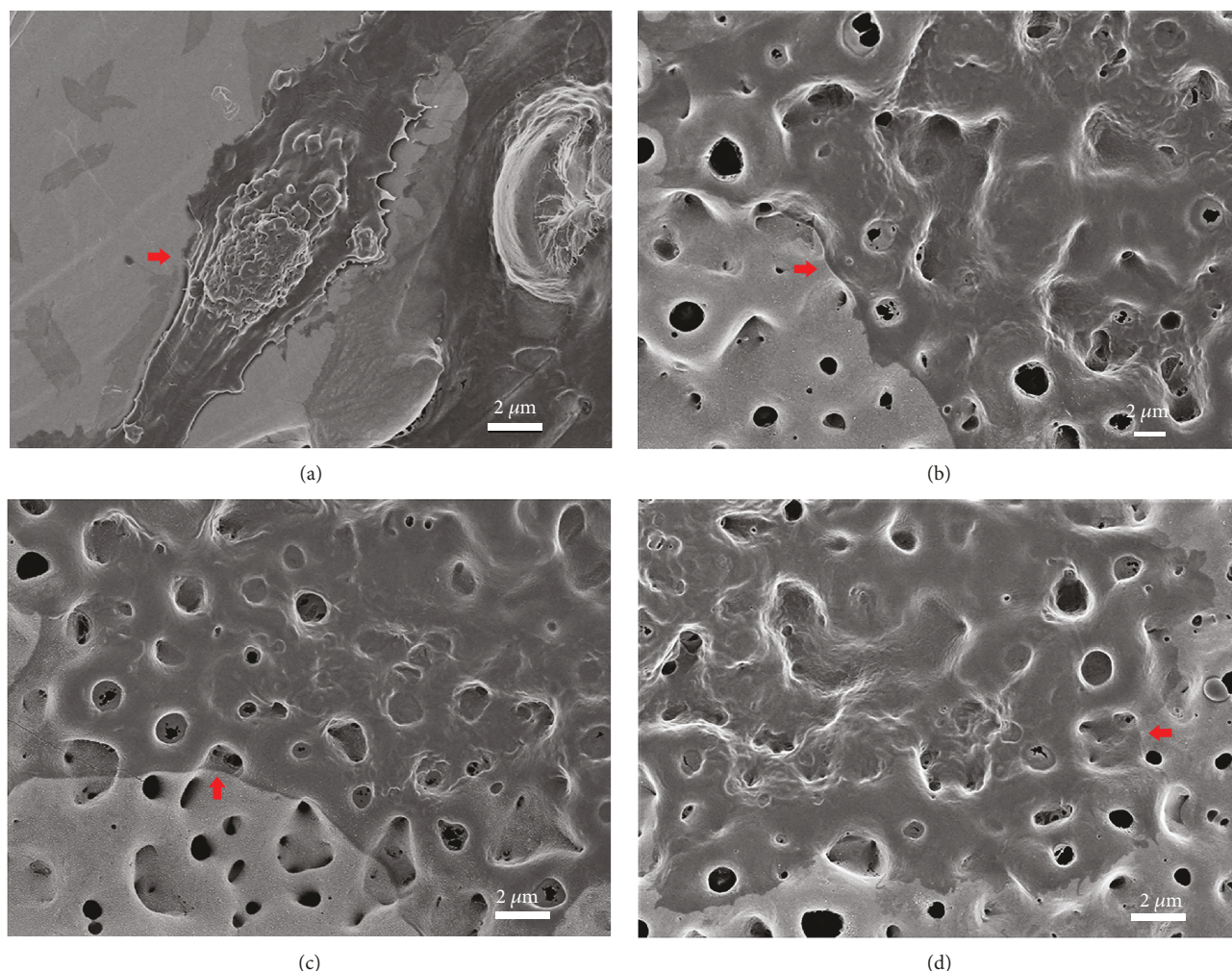


FIGURE 8: SEM morphology of MC3T3-E1 cells cultured on each sample after 2 hours (scale bar of (a–d) = 2 μm). Red arrows point out the position of cells. SLM (a), MAO (b), 1 mM-Zn (c), and 100 μM -Zn (d).

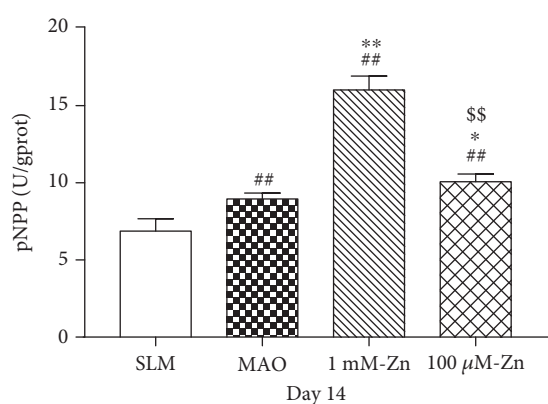


FIGURE 9: ALP activity of MC3T3-e1 cells on each sample after 14 days of incubation. # $P < 0.05$ and ## $P < 0.01$ compared with SLM; * $P < 0.05$ and ** $P < 0.01$ compared with MAO; \$ $P < 0.05$ and \$\$ $P < 0.01$ compared with 1 mM-Zn.

for cell adhesion. Cells were observed extensively spreading out on Zn-incorporated coating surfaces. In addition, first-day CCK-8 results revealed that cells proliferate better on

Zn-incorporated samples when compared to SLM and MAO samples, likely due to the outstanding hydrophilicity and special micro-nano topography of the former groups. After incubation for 7 days, 100 μM -Zn samples were found to be the most ideal for cell proliferation. MAO and 1 mM-Zn samples exhibited similar biological characteristics and were both superior to SLM specimens.

ALP activity, an early marker of osteogenesis, was markedly increased on Zn-incorporated specimens compared to SLM and MAO samples. Moreover, 1 mM-Zn samples expressed the highest ALP activity after 14 days, suggesting that higher loading of incorporated Zn exerts positive effects on cellular differentiation as long as Zn content does not exceed a concentration that is biologically safe. These results were not completely in accordance with the cell proliferation assays in which 100 μM -Zn samples showed the best proliferation ability. This might be because a high content of ZnO from Zn-incorporated samples could not only enhance ALP activity but also decrease the proliferation of cells in some degree at the same time despite the suitable surface topography, roughness, and hydrophilicity, which drew no conflicting conclusions to these two results.

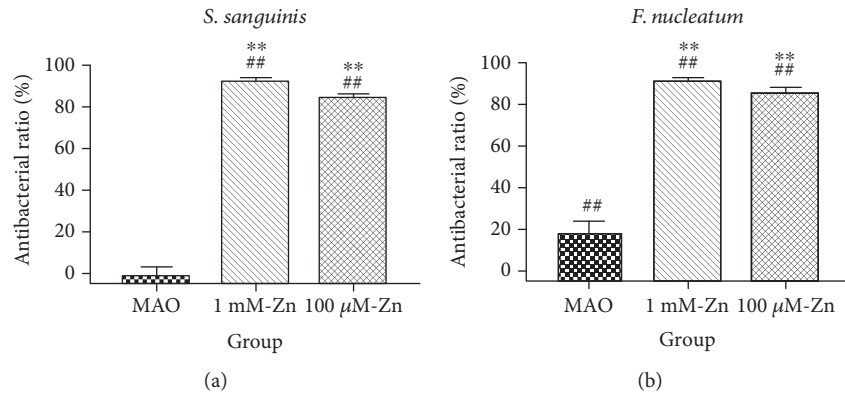


FIGURE 10: Antibacterial ratio of *S. sanguinis* and *F. nucleatum* on the surfaces of each sample after 24 h of incubation. #*P* < 0.05 and ##*P* < 0.01 compared with the baseline (0% as SLM group). **P* < 0.05 and ***P* < 0.01 compared with MAO.

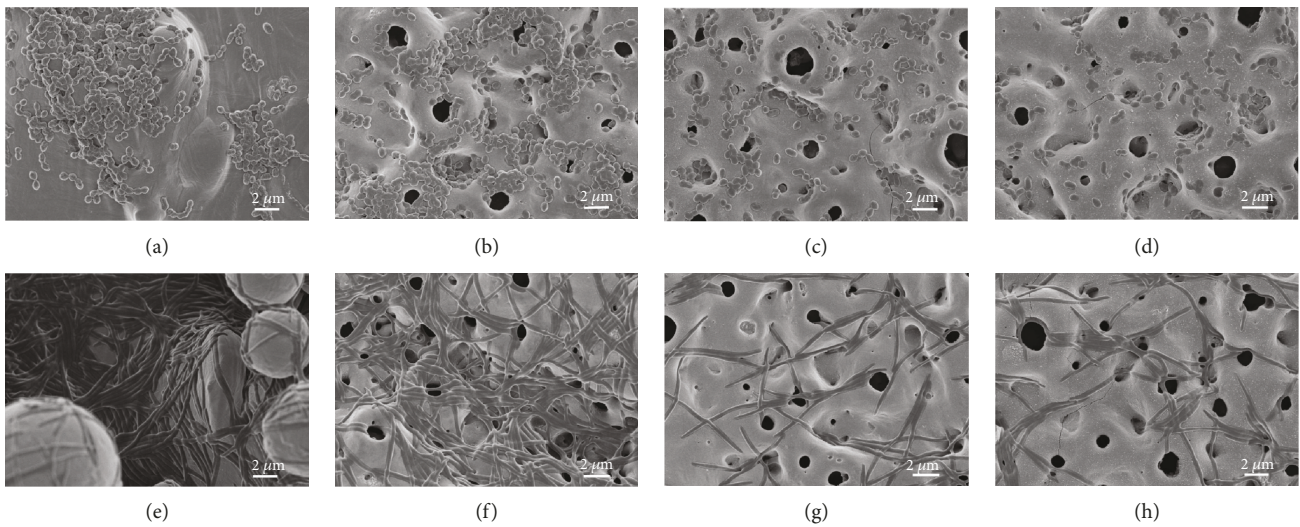


FIGURE 11: SEM morphology of *S. sanguinis* and *F. nucleatum* adhesion on the surface of each sample after 24 hours of incubation (scale bar of (a–h) = 2 μm). SEM of *S. sanguinis*: SLM (a), MAO (b), 1 mM-Zn (c), and 100 μM-Zn (d), and SEM of *F. nucleatum*: SLM (e), MAO (f), 1 mM-Zn (g), and 100 μM-Zn (h).

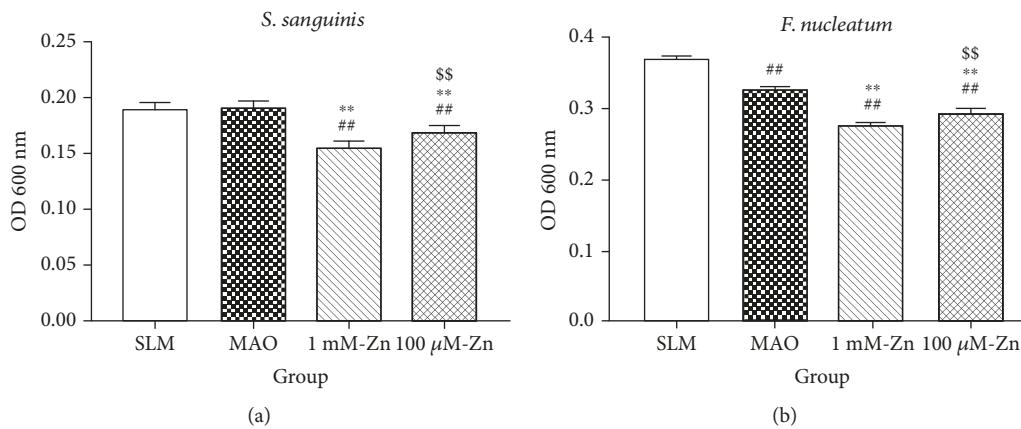


FIGURE 12: The bacteria density in supernatant of *S. sanguinis* and *F. nucleatum* after 24 hours of incubation. *S. sanguinis* (a) and *F. nucleatum* (b). #*P* < 0.05 and ##*P* < 0.01 compared with SLM; **P* < 0.05 and ***P* < 0.01 compared with MAO; and §*P* < 0.05 and §§*P* < 0.01 compared with 1 mM-Zn.

With MAO and subsequent hydrothermal treatment, varying quantities of Zn can be incorporated into TiO₂ coatings to modify the native SLM surface. Compared with SLM and MAO specimens, Zn-incorporated samples exhibited better antibacterial activity and cytocompatibility.

Further studies should focus on animal experiments to evaluate whether this Zn-incorporated modification possesses similar biological capabilities in vivo as it does in vitro, thus establishing a solid foundation for future clinical application.

5. Conclusions

In this study, a novel micro-nano topographic coating incorporated with Zn was fabricated on the rough SLM surface by MAO and hydrothermal treatment. Due to a sustained release of Zn ions and superior hydrophilicity, Zn-incorporated samples highly promoted the adhesion, proliferation, and differentiation of MC3T3-E1 cells when compared to SLM and MAO samples. This modified surface also exhibited outstanding antibacterial effects against oral pathogenic flora (*S. sanguinis* and *F. nucleatum*), potentially significantly reducing the risk of peri-implant inflammation and ensuring long-term implant survival. Our study thus contributes to the advancement of customized biomedical implant fabrication with SLM technology.

Data Availability

All data included in this study are available upon request by contact with the corresponding author.

Conflicts of Interest

There is no conflict of interest regarding the publication of this paper.

Authors' Contributions

Fan Wu and Ruogu Xu contributed equally to this work.

Acknowledgments

The authors are sincerely grateful to all the research staff members at the Department of Oral Implantology, Guanghua School of Stomatology, and the Institute of Advanced Technology, Chinese Academy of Science. This work is supported by the National Natural Science Foundation of China (81501600) and Science and Technology Major Project of Guangdong Province (2017B090912004).

References

- [1] M. Dierens, S. Vandeweghe, J. Kisch, K. Nilner, and H. de Bruyn, "Long-term follow-up of turned single implants placed in periodontally healthy patients after 16-22 years: radiographic and peri-implant outcome," *Clinical Oral Implants Research*, vol. 23, no. 2, pp. 197–204, 2012.
- [2] S. S. Al-Johany, M. D. al Amri, S. Alsaeed, and B. Alalola, "Dental implant length and diameter: a proposed classification scheme," *Journal of Prosthodontics*, vol. 26, no. 3, pp. 252–260, 2017.
- [3] J. Y. Chen, Z. Z. Zhang, X. S. Chen, C. Zhang, G. Zhang, and Z. Xu, "Design and manufacture of customized dental implants by using reverse engineering and selective laser melting technology," *The Journal of Prosthetic Dentistry*, vol. 112, no. 5, pp. 1088–1095.e1, 2014.
- [4] M. Figliuzzi, F. Mangano, and C. Mangano, "A novel root analogue dental implant using CT scan and CAD/CAM: selective laser melting technology," *International Journal of Oral & Maxillofacial Surgery*, vol. 41, no. 7, pp. 858–862, 2012.
- [5] M. Rana, M. M. Gellrich, and N. C. Gellrich, "Customised reconstruction of the orbital wall and engineering of selective laser melting (SLM) core implants," *British Journal of Oral and Maxillofacial Surgery*, vol. 53, no. 2, pp. 208–209, 2015.
- [6] Z. J. Wally, A. M. Haque, A. Feteira, F. Claeysens, R. Goodall, and G. C. Reilly, "Selective laser melting processed Ti6Al4V lattices with graded porosities for dental applications," *Journal of the Mechanical Behavior of Biomedical Materials*, vol. 90, pp. 20–29, 2019.
- [7] P. H. Warnke, T. Douglas, P. Wollny et al., "Rapid prototyping: porous titanium alloy scaffolds produced by selective laser melting for bone tissue engineering," *Tissue Engineering Part C: Methods*, vol. 15, no. 2, pp. 115–124, 2009.
- [8] A. Shaoki, J. Y. Xu, H. P. Sun et al., "Osseointegration of three-dimensional designed titanium implants manufactured by selective laser melting," *Biofabrication*, vol. 8, no. 4, article 045014, 2016.
- [9] H. Wang, B. J. Zhao, C. K. Liu, C. Wang, X. Tan, and M. Hu, "A comparison of biocompatibility of a titanium alloy fabricated by electron beam melting and selective laser melting," *PLoS One*, vol. 11, no. 7, article e0158513, 2016.
- [10] M. de Wild, R. Schumacher, K. Mayer et al., "Bone regeneration by the osteoconductivity of porous titanium implants manufactured by selective laser melting: a histological and micro computed tomography study in the rabbit," *Tissue Engineering Part A*, vol. 19, no. 23–24, pp. 2645–2654, 2013.
- [11] J. Vaithilingam, E. Prina, R. D. Goodridge et al., "Surface chemistry of Ti6Al4V components fabricated using selective laser melting for biomedical applications," *Materials Science and Engineering: C*, vol. 67, pp. 294–303, 2016.
- [12] X. C. Hu, R. Xu, X. Yu et al., "Enhanced antibacterial efficacy of selective laser melting titanium surface with nanophase calcium phosphate embedded to TiO₂ nanotubes," *Biomedical Materials*, vol. 13, no. 4, article 045015, 2018.
- [13] I. A. J. van Hengel, M. Riool, L. E. Fratila-Apachitei et al., "Selective laser melting porous metallic implants with immobilized silver nanoparticles kill and prevent biofilm formation by methicillin-resistant *Staphylococcus aureus*," *Biomaterials*, vol. 140, pp. 1–15, 2017.
- [14] J. Y. Xu, X. S. Chen, C. Y. Zhang, Y. Liu, J. Wang, and F. L. Deng, "Improved bioactivity of selective laser melting titanium: surface modification with micro-/nano-textured hierarchical topography and bone regeneration performance evaluation," *Materials Science and Engineering: C*, vol. 68, pp. 229–240, 2016.
- [15] R. G. Xu, X. C. Hu, X. L. Yu et al., "Micro-/nano-topography of selective laser melting titanium enhances adhesion and proliferation and regulates adhesion-related gene expressions of human gingival fibroblasts and human gingival epithelial cells," *International Journal of Nanomedicine*, vol. 13, pp. 5045–5057, 2018.

- [16] M. Echeverry-Rendón, O. Galvis, R. Aguirre, S. Robledo, J. G. Castaño, and F. Echeverría, "Modification of titanium alloys surface properties by plasma electrolytic oxidation (PEO) and influence on biological response," *Journal of Materials Science: Materials in Medicine*, vol. 28, no. 11, p. 169, 2017.
- [17] I. da Silva Vieira Marques, V. A. R. Barão, N. C. da Cruz et al., "Electrochemical behavior of bioactive coatings on cp-Ti surface for dental application," *Corrosion Science*, vol. 100, pp. 133–146, 2015.
- [18] A. Kazek-Kęsik, M. Krok-Borkowicz, E. Pamuła, and W. Simka, "Electrochemical and biological characterization of coatings formed on Ti-15Mo alloy by plasma electrolytic oxidation," *Materials Science and Engineering: C*, vol. 43, pp. 172–181, 2014.
- [19] F. Deng, W. Z. Zhang, P. F. Zhang, C. Liu, and J. Ling, "Improvement in the morphology of micro-arc oxidised titanium surfaces: a new process to increase osteoblast response," *Materials Science and Engineering: C*, vol. 30, no. 1, pp. 141–147, 2010.
- [20] J. Derks and C. Tomasi, "Peri-implant health and disease. A systematic review of current epidemiology," *Journal of Clinical Periodontology*, vol. 42, Suppl 16, pp. S158–S171, 2015.
- [21] J. W. Costerton, P. S. Stewart, and E. P. Greenberg, "Bacterial biofilms: a common cause of persistent infections," *Science*, vol. 284, no. 5418, pp. 1318–1322, 1999.
- [22] J. Wang, G. F. Wu, X. W. Liu, G. Sun, D. Li, and H. Wei, "A decomposable silica-based antibacterial coating for percutaneous titanium implant," *International Journal of Nanomedicine*, vol. 12, pp. 371–379, 2017.
- [23] K. Dydak, A. Junka, P. Szymczyk et al., "Development and biological evaluation of Ti6Al7Nb scaffold implants coated with gentamycin-saturated bacterial cellulose biomaterial," *PLoS One*, vol. 13, no. 10, article e0205205, 2018.
- [24] A. S. Prasad, "Discovery of human zinc deficiency: its impact on human health and disease," *Advances in Nutrition*, vol. 4, no. 2, pp. 176–190, 2013.
- [25] K. B. Hadley, S. M. Newman, and J. R. Hunt, "Dietary zinc reduces osteoclast resorption activities and increases markers of osteoblast differentiation, matrix maturation, and mineralization in the long bones of growing rats," *The Journal of Nutritional Biochemistry*, vol. 21, no. 4, pp. 297–303, 2010.
- [26] H. Cheng, L. Mao, L. Wang et al., "Bidirectional regulation of zinc embedded titania nanorods: antibiosis and osteoblastic cell growth," *RSC Advances*, vol. 5, no. 19, pp. 14470–14481, 2015.
- [27] H. Hu, W. Zhang, Y. Qiao, X. Jiang, X. Liu, and C. Ding, "Antibacterial activity and increased bone marrow stem cell functions of Zn-incorporated TiO₂ coatings on titanium," *Acta Biomaterialia*, vol. 8, no. 2, pp. 904–915, 2012.
- [28] J. Y. Zhang, H. J. Ai, and M. Qi, "Osteoblast growth on the surface of porous Zn-containing HA/TiO₂ hybrid coatings on Ti substrate by MAO plus sol-gel methods," *Surface and Coating Technology*, vol. 228, Supplement 1, pp. S202–S205, 2013.
- [29] K. F. Huo, X. M. Zhang, H. R. Wang, L. Zhao, X. Liu, and P. K. Chu, "Osteogenic activity and antibacterial effects on titanium surfaces modified with Zn-incorporated nanotube arrays," *Biomaterials*, vol. 34, no. 13, pp. 3467–3478, 2013.
- [30] Y. Q. Qiao, W. J. Zhang, P. Tian et al., "Stimulation of bone growth following zinc incorporation into biomaterials," *Biomaterials*, vol. 35, no. 25, pp. 6882–6897, 2014.
- [31] A. Sirelkhatim, S. Mahmud, A. Seeni et al., "Review on zinc oxide nanoparticles: antibacterial activity and toxicity mechanism," *Nano-Micro Letters*, vol. 7, no. 3, pp. 219–242, 2015.
- [32] A. Kawakubo, T. Matsunaga, H. Ishizaki, S. Yamada, and Y. Hayashi, "Zinc as an essential trace element in the acceleration of matrix vesicles-mediated mineral deposition," *Microscopy Research and Technique*, vol. 74, no. 12, pp. 1161–1165, 2011.
- [33] X.-M. Zhuang, B. Zhou, J. L. Ouyang et al., "Enhanced MC3T3-E1 preosteoblast response and bone formation on the addition of nano-needle and nano-porous features to microtopographical titanium surfaces," *Biomedical Materials*, vol. 9, no. 4, article 045001, 2014.
- [34] W. J. Landis and J. R. Martin, "X-ray photoelectron spectroscopy applied to gold-decorated mineral standards of biological interest," *Journal of Vacuum Science & Technology A: Vacuum, Surfaces, and Films*, vol. 2, no. 2, pp. 1108–1111, 1984.
- [35] H. Y. Cheng, Z. Gong, H. Hu et al., "Design of alveolate Se-inserted TiO₂ and its effect on osteosarcoma cells and osteoblasts," *Journal of Materials Chemistry B*, vol. 5, no. 10, pp. 1988–2001, 2017.
- [36] M. Zhang, H. Y. Cheng, Z. N. Gong et al., "Fabrication of chitosan-18β-glycyrrhetic acid modified titanium implants with nanorod arrays for suppression of osteosarcoma growth and improvement of osteoblasts activity," *Advanced Functional Materials*, vol. 27, no. 43, article 1703932, 2017.
- [37] Z. N. Gong, H. Cheng, M. Zhang et al., "Osteogenic activity and angiogenesis of a SrTiO₃ nano-gridding structure on titanium surface," *Journal of Materials Chemistry B*, vol. 5, no. 3, pp. 537–552, 2017.
- [38] R. V. Chernozem, M. A. Surmeneva, B. Krause et al., "Functionalization of titania nanotubes with electrophoretically deposited silver and calcium phosphate nanoparticles: structure, composition and antibacterial assay," *Materials Science and Engineering: C*, vol. 97, pp. 420–430, 2019.
- [39] T. Albrektsson and A. Wennerberg, "Oral implant surfaces: part 1—review focusing on topographic and chemical properties of different surfaces and in vivo responses to them," *The International Journal of Prosthodontics*, vol. 17, no. 5, pp. 536–543, 2004.
- [40] H. J. Rønold and J. E. Ellingsen, "Effect of micro-roughness produced by TiO₂ blasting—tensile testing of bone attachment by using coin-shaped implants," *Biomaterials*, vol. 23, no. 21, pp. 4211–4219, 2002.
- [41] H. J. Rønold, S. P. Lyngstadaas, and J. E. Ellingsen, "Analysing the optimal value for titanium implant roughness in bone attachment using a tensile test," *Biomaterials*, vol. 24, no. 25, pp. 4559–4564, 2003.
- [42] C. M. L. Bollen, W. Papaioanno, J. van Eldere, E. Schepers, M. Quirynen, and D. van Steenberghe, "The influence of abutment surface roughness on plaque accumulation and peri-implant mucositis," *Clinical Oral Implants Research*, vol. 7, no. 3, pp. 201–211, 1996.
- [43] W. Teughels, N. van Assche, I. Sliepen, and M. Quirynen, "Effect of material characteristics and/or surface topography on biofilm development," *Clinical Oral Implants Research*, vol. 17, no. S2, pp. 68–81, 2006.
- [44] J. H. Wei, M. Yoshinari, S. Takemoto et al., "Adhesion of mouse fibroblasts on hexamethyldisiloxane surfaces with wide range of wettability," *Journal of Biomedical Materials Research Part B: Applied Biomaterials*, vol. 81B, no. 1, pp. 66–75, 2007.

- [45] N. P. Lang, G. E. Salvi, G. Huynh-Ba, S. Ivanovski, N. Donos, and D. D. Bosshardt, "Early osseointegration to hydrophilic and hydrophobic implant surfaces in humans," *Clinical Oral Implants Research*, vol. 22, no. 4, pp. 349–356, 2011.
- [46] N. Donos, S. Hamlet, N. P. Lang et al., "Gene expression profile of osseointegration of a hydrophilic compared with a hydrophobic microrough implant surface," *Clinical Oral Implants Research*, vol. 22, no. 4, pp. 365–372, 2011.
- [47] S. C. Sartoretto, J. A. Calasans-Maia, Y. O. Costa, R. S. Louro, J. M. Granjeiro, and M. D. Calasans-Maia, "Accelerated healing period with hydrophilic implant placed in sheep tibia," *Brazilian Dental Journal*, vol. 28, no. 5, pp. 559–565, 2017.
- [48] A. W. J. Pelt, H. C. Mei, H. J. Busscher, J. Arends, and A. H. Weerkamp, "Surface free energies of oral streptococci," *FEMS Microbiology Letters*, vol. 25, no. 2-3, pp. 279–282, 1984.
- [49] M. Astasov-Frauenhoffer, S. Glauser, J. Fischer, F. Schmidli, T. Waltimo, and N. Rohr, "Biofilm formation on restorative materials and resin composite cements," *Dental Materials*, vol. 34, no. 11, pp. 1702–1709, 2018.
- [50] G. Applerot, A. Lipovsky, R. Dror et al., "Enhanced antibacterial activity of nanocrystalline ZnO due to increased ROS-mediated cell injury," *Advanced Functional Materials*, vol. 19, no. 6, pp. 842–852, 2009.
- [51] A. Ratn, R. Prasad, Y. Awasthi, M. Kumar, A. Misra, and S. P. Trivedi, "Zn²⁺ induced molecular responses associated with oxidative stress, DNA damage and histopathological lesions in liver and kidney of the fish, *Channa punctatus* (Bloch, 1793)," *Ecotoxicology and Environmental Safety*, vol. 151, pp. 10–20, 2018.
- [52] A. G. Rodríguez-Hernández, A. Juárez, E. Engel, and F. J. Gil, "*Streptococcus sanguinis* adhesion on titanium rough surfaces: effect of shot-blasting particles," *Journal of Materials Science: Materials in Medicine*, vol. 22, no. 8, pp. 1913–1922, 2011.
- [53] B. Rosan and R. J. Lamont, "Dental plaque formation," *Microbes and Infection*, vol. 2, no. 13, pp. 1599–1607, 2000.
- [54] A. Mombelli and N. P. Lang, "Microbial aspects of implant dentistry," *Periodontology 2000*, vol. 4, no. 1, pp. 74–80, 1994.
- [55] A. O. Matos, A. P. Ricomini-Filho, T. Beline et al., "Three-species biofilm model onto plasma-treated titanium implant surface," *Colloids and Surfaces B: Biointerfaces*, vol. 152, pp. 354–366, 2017.
- [56] Z. X. Zhang, B. B. Gu, W. J. Zhang, G. Kan, and J. Sun, "The enhanced characteristics of osteoblast adhesion to porous zinc-TiO₂ coating prepared by plasma electrolytic oxidation," *Applied Surface Science*, vol. 258, no. 17, pp. 6504–6511, 2012.
- [57] M. Hie and I. Tsukamoto, "Administration of zinc inhibits osteoclastogenesis through the suppression of RANK expression in bone," *European Journal of Pharmacology*, vol. 668, no. 1-2, pp. 140–146, 2011.
- [58] A. Yamamoto, R. Honma, and M. Sumita, "Cytotoxicity evaluation of 43 metal salts using murine fibroblasts and osteoblastic cells," *Journal of Biomedical Materials Research*, vol. 39, no. 2, pp. 331–340, 1998.
- [59] A. Ito, H. Kawamura, M. Otsuka et al., "Zinc-releasing calcium phosphate for stimulating bone formation," *Materials Science and Engineering: C*, vol. 22, no. 1, pp. 21–25, 2002.

